Control of the laser frequency in the Virgo interferometer

Astroparticle Physics 164 (2025) 103028

Contents lists available at ScienceDirect

Astroparticle Physics

journal homepage: www.elsevier.com/locate/astropartphys

Control of the laser frequency in the Virgo interferometer: Dynamic noise budgeting for controller optimization

Mathyn van Dael [a,b,*], Julia Casanueva [c], Gert Witvoet [a,d], Bas Swinkels [b], Diego Bersanetti [e], Manuel Pinto [c], Paolo Ruggi [c], Maddalena Mantovani [c], Camilla de Rossi [c], Piernicola Spinicelli [c], Mattia Boldrini [f], Tom Oomen [g]

[a] Eindhoven University of Technology, department of Mechanical Engineering, Control Systems Technology, Eindhoven, Postbus 513, 5600 MB, The Netherlands
[b] Nikhef, Science Park 105, Amsterdam, 1098 XG, The Netherlands
[c] European Gravitational Observatory (EGO), Cascina, I-56021, Pisa, Italy
[d] TNO, Optomechatronics Department, Delft, The Netherlands
[e] INFN, Sezione di Genova, Genova, I-16146, Italy
[f] INFN, Sezione di Roma, Piazzale Aldo Moro 2, Roma, I-00185, Italy
[g] Delft University of Technology, Delft Center for Systems and Control, Delft, The Netherlands

ARTICLE INFO

Keywords:
Advanced Virgo Plus
Laser frequency stabilization
Noise budget
Systematic control design
$\mathcal{H}_2$ synthesis
Gravitational Waves

ABSTRACT

This paper presents a framework for the derivation of a noise budget and the subsequent utilization in the optimization of the control design, using the laser frequency stabilization loop in the Virgo interferometer, which is a complex nested feedback system, as an experimental case study. First, the system dynamics and noise sources are modeled and experimentally verified to produce the noise budget, after which an optimization problem using the $\mathcal{H}_2$ norm is formulated and tailored to the specific design requirements for the detector. The structure of the synthesized controller is then used to produce an improved control design. Experimental verification of the developed controller on the Virgo interferometer shows roughly a factor 3 reduction in root-mean-square error, illustrating the effectiveness of the presented method.

1. Introduction

The laser frequency stabilization system, consisting of a set of complex nested feedback loops, is an essential subsystem in the Advanced Virgo Plus (AdV+) [1] Gravitational Wave detector as it is responsible for reducing the laser frequency fluctuations by more than 7 orders of magnitude. Optimizing such complex subsystems requires an accurate noise budget, which shows the contribution of each disturbance to the output of the system as a function of frequency content, see e.g., [2,3]. The development of such a noise budget requires modeling both the system dynamics as well as the external disturbances. For complex subsystems with e.g., nested feedback loops such as the laser frequency stabilization loop, the development of a noise budget can be a complex and time-consuming procedure and it is furthermore not necessarily straightforward how to incorporate the noise budget in the optimization of the control design.

On the modeling side of the laser frequency stabilization loop, two of the feedback loops have been individually modeled in [4,5] and a noise budget has also been developed for one of these loops in [5]. The third feedback loop has also been modeled in [6], but a complete system model integrating the three feedback loops as well as a noise budget for the complete system is still missing. In terms of optimizing control designs in Gravitational Wave detectors, Thomas et al. [7], Schütte [8], Trozzo [9] and Beker et al. [10] have worked on using synthesis methods to optimize the control design. In e.g., [8,11], modern control techniques such as $\mathcal{H}_2$ and $\mathcal{H}_\infty$ are explored for a suspension system, illustrating a systematic design procedure to improve the control design. The noise budgets are however not explicitly considered in the optimization and instead, weighting functions are developed using system insight, which is not necessarily optimal. In [10], the noise budget is also incorporated in the optimization to synthesize an Linear–Quadratic–Gaussian controller, showing promising improvements in performance. The optimization does however not consider the frequency-dependent coupling to the sensitivity of the detector, which is essential to incorporate in the optimization for most subsystems.

Although parts of the laser frequency stabilization loop have already been modeled, a systematic approach is essential for meeting

* Corresponding author at: Eindhoven University of Technology, department of Mechanical Engineering, Control Systems Technology, Eindhoven, Postbus 513, 5600 MB, The Netherlands.
E-mail address: m.r.v.dael@tue.nl (M. van Dael).

https://doi.org/10.1016/j.astropartphys.2024.103028
Received 7 March 2024; Received in revised form 22 July 2024; Accepted 5 August 2024
Available online 8 August 2024

the performance requirements. The aim of this paper is to present a systematic design procedure that incorporates the noise budget in the optimization of the control design, where also frequency-dependent design considerations are included in the optimization.

The main contributions of this paper are therefore three-fold. The first contribution is the development and experimental verification of the model and noise budget for this control system. The second contribution is to utilize controller synthesis to derive an improved control design, where the noise budget as well as other system requirements are incorporated into the optimization. The final contribution is to illustrate the potential of control design tools developed in the Control community, in this case, controller optimization using $\mathcal{H}_2$ synthesis, for challenges in the Gravitational Wave community and present them as a systematic procedure.

The outline of this paper is as follows. In Section 2 an overview of the detector and the control system for the laser frequency stabilization in AdV+ is presented, as well as the problem formulation. The modeling procedure for this subsystem is presented in Section 3, and the development and verification of the noise budget is presented in Section 4. The optimization of one of the controllers in the subsystem is presented in Section 5, and experimental results on AdV+ using the new controller are presented in Section 6. Section 7 finally contains the conclusion and discussion.

2. System overview and problem formulation

This section presents an overview of the system and the problem addressed in this paper is formalized.

2.1. System description

The AdV+ detector, shown in Fig. 1(a), is a dual-recycled Michelson interferometer [1] with two 3 km long Fabry–Perot cavities (x_W, x_N in Fig. 1(a)). In total, 5 so-called longitudinal Degrees of Freedom (DoFs) [12] are actively controlled. Of these, the Differential Arm (DARM) DoF, defined by

$$x_{\text{DARM}} = x_W - x_N, \tag{1}$$

is the most important since this DoF changes in length with the passing of a Gravitational Wave. Most of these DoFs are actively controlled by using demodulated error signals to derive a locally valid error signal [13], which is subsequently used to apply small forces on one or more of the mirrors and change the cavity lengths, see e.g., [12].

The Common Arm (CARM) of the Fabry–Perot cavities is given by

$$x_{\text{CARM}} = \frac{x_W + x_N}{2}, \tag{2}$$

and requires a more convoluted control approach since a higher level of attenuation is required over a broader frequency range. The resonance condition for a Fabry–Perot cavity is given by

$$x = N \cdot \frac{\lambda}{2}, \tag{3}$$

with x the cavity length, λ the wavelength of the laser and N an integer number. For the arm cavities to be in resonance, the arm lengths must thus be an integer multiple of half the wavelength of the laser. Both the cavity length and laser frequency fluctuations are orders higher with respect to the design requirement, therefore requiring very fast feedback loops that actively ensure that the resonance condition of the Fabry–Perot cavities is satisfied. The strategy used in AdV+ to satisfy (3) is explained next.

2.2. Control system for CARM

The objective of the control scheme for CARM is to stabilize the laser frequency fluctuations by more than 7 orders of magnitude [4] as well as to stabilize the root-mean-square (RMS) arm length fluctuations by more than 2 orders of magnitude. Stabilization of the laser frequency is required since CARM is the most sensitive DoF to frequency noise and these fluctuations directly couple to the DARM degree of freedom in the detection band (> 10 Hz) due to asymmetries in the optics of the detector. The minimization of the RMS arm length fluctuations is needed to minimize the noise inside the detection band through non-linear couplings [14].

In Fig. 1(a), the optical configuration of AdV+ is depicted together with the control scheme used to stabilize the laser frequency fluctuations and control the CARM DoF, where the purple blocks K_{PS}, K_{MC}, K_{SSFS} and K_{RFC} are controllers. The control system consists of three nested loops that are highlighted by the colored, dashed, rectangular boxes. The first loop, commonly referred to as the Pre-Stabilization (PS) loop, highlighted in orange, is used to stabilize the laser frequency fluctuations. This is done by locking the laser onto the Input Mode Cleaner (IMC) cavity, where the photodiode in reflection of the IMC provides an error signal using the Pound–Drever–Hall technique [13] with demodulated signals to control the laser frequency with a Unity Gain Frequency (UGF) of roughly 110 kHz. The second loop, highlighted by the blue rectangle and commonly referred to as the Second Stage of Frequency Stabilization (SSFS) loop, subsequently locks the laser on the arm cavities since one of the control objectives is the relative stability between the laser frequency and arm cavity lengths. To do so, the B4 photodiode is used as an error signal (using the same method as for the IMC error signal) and the actuation is done using two different actuation branches. At low frequencies (< 200 Hz), a correction is sent to the IMC mirror which changes the resonance frequency of the cavity and forces the inner PS loop to follow, hence adjusting the laser frequency accordingly. Above 200 Hz, the correction for the laser frequency is directly given as a setpoint to the PS loop. The UGF of the SSFS loop is around 7 kHz.

Above 10 Hz, both the IMC and arm cavities provide a stable length reference for the laser. However, below this frequency, the mirrors directly follow the ground motion, which is orders higher than the mirror motions above 10 Hz as the ground motion coupling to the mirrors is attenuated by more than 10 orders of magnitude above this frequency. As a consequence of the two feedback loops, the laser directly follows the cavity motions and hence the ground motion, thus introducing large laser frequency fluctuations below 10 Hz. To lower these fluctuations, a third loop is used that measures the laser frequency fluctuation using a photodiode in reflection of the Reference Cavity (RFC), which is a monolithic cavity constructed from Ultra Low Expansion glass. Using this error signal, a common correction is sent to the arm cavity end mirrors with a UGF of around 2 Hz. This loop, commonly referred to as the RFC loop, reduces the cavity length fluctuations and consequently also the laser frequency fluctuations.

Laser frequency fluctuations couple linearly to the detector sensitivity and the present control configuration reaches the design requirements for this noise inside the detection band of AdV+ (10 to 10 kHz). The laser frequency fluctuations also couple non-linearly to the detector sensitivity [15], i.e., low-frequency fluctuations (< 10 Hz) may introduce noise in the detection band of the detector. To minimize this noise affecting the sensitivity, either the non-linear coupling or the RMS laser frequency noise can be reduced. In AdV+, the non-linear coupling is minimized through several methods, e.g., by optimizing the alignment of the optics, which may go at the expense of the increased coupling of other noise sources. Further reduction of the RMS laser frequency fluctuations is therefore beneficial as this relaxes the requirements on e.g., the alignment of the optics.

2.3. Problem formulation

The dominant driver of the RMS of the laser frequency fluctuations is the ground motion. The RFC loop has been introduced to mitigate these fluctuations, but the bandwidth of this loop is limited to roughly

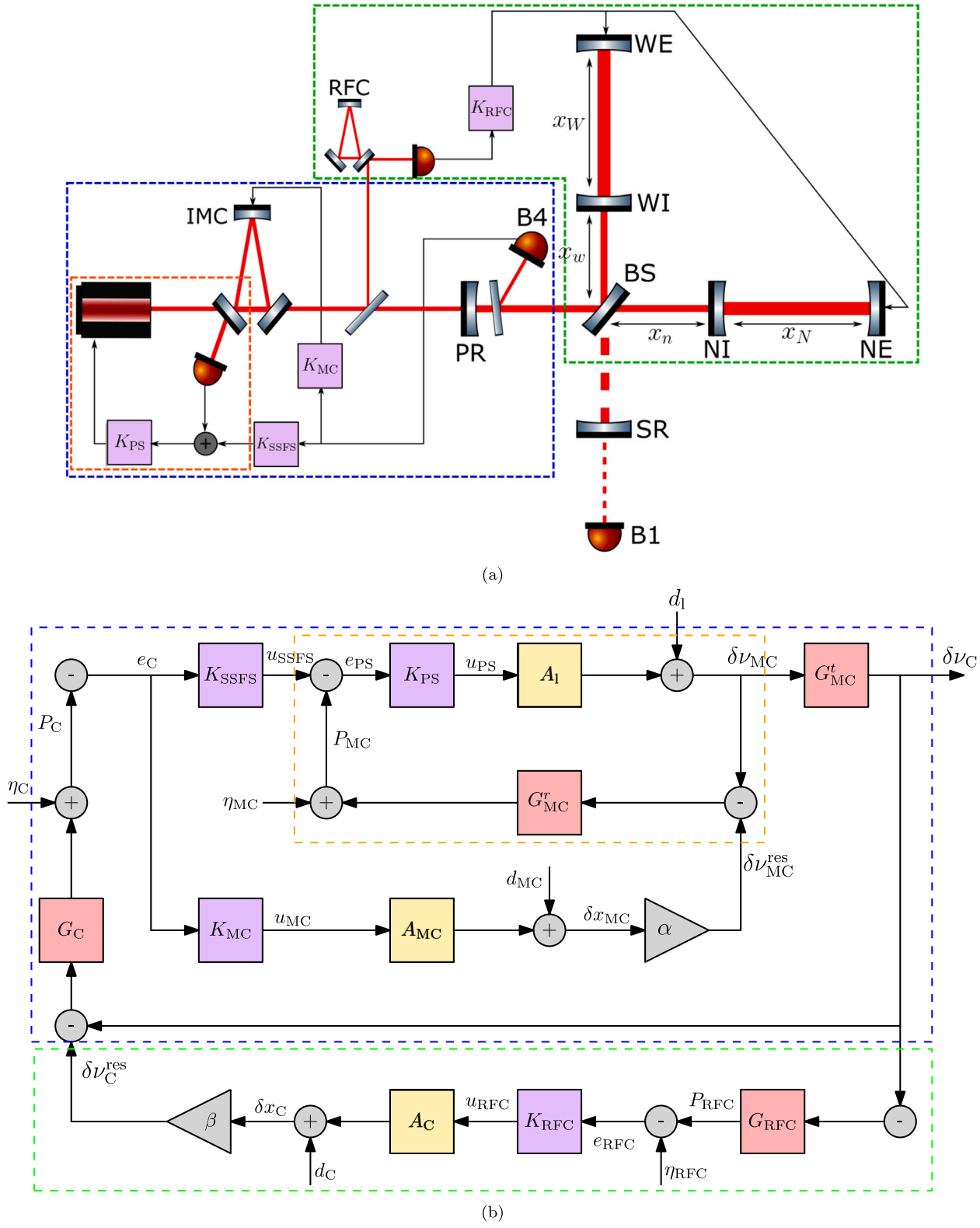

Fig. 1. (a) Part of the optical configuration of AdV+ for the next science run, including the control architecture for the laser stabilization and CARM loop. The B1 photodiode measures the interference pattern between the two arms (x_W and x_N), which change in length with opposite signs when a Gravitational Wave passes. The two arms x_W and x_N are 3 km long in the case of AdV+. (b) Block diagram of the control scheme for the laser frequency stabilization and CARM. The purple blocks denote controllers, the red blocks denote optical transfer functions and the yellow blocks denote mechanical transfer functions. The three nested loops, highlighted by the rectangular boxes, correspond to the same loops as presented as in (a).

Table 1
Overview of the variables used in the block diagram.

Variable	Description
$\delta\nu_C$	Laser frequency fluctuations entering arm cavities [Hz]
$\delta\nu_{MC}$	Laser frequency fluctuations entering Input Mode Cleaner [Hz]
δx_C	Length fluctuations of arm cavities [m]
δx_{MC}	Length fluctuations of Input Mode Cleaner cavity [m]
$\delta\nu_C^{res}$	Arm cavity resonance frequency fluctuations [Hz]
$\delta\nu_{MC}^{res}$	Input Mode Cleaner resonance frequency fluctuations [Hz]
$u_\bullet$	Correction signals for actuators [V]
$P_\bullet$	Signals on photodiodes [W]
$e_\bullet$	Error signals [W]
d_l	Free running laser frequency noise [Hz]
d_{MC}	Seismic noise affecting IMC length [m]
d_C	Seismic noise affecting arm cavity length [m]
η_{MC}	Sensor noise on IMC photodiode [W]
η_C	Sensor noise on B4 photodiode [W]
η_{RFC}	Sensor noise on RFC photodiode [W]

2 Hz to avoid introducing noise in the detection band, thus also limiting the low-frequency attenuation of ground motion. The problem addressed in this paper is therefore how to optimize the control design of K_{RFC} to further reduce the RMS laser frequency fluctuations.

The complete control system of the CARM DoF consists of a set of nested loops, making it difficult to identify the different control design considerations, i.e., how each of the noise sources couple to the output. Having a noise budget that accurately models the couplings of the different noise sources to the output allows for easier optimization of the control design. The first part of this paper will therefore present the derivation and verification of a model and noise budget for the complete control system of CARM.

While noise budgets are often made to identify opportunities for improving the control systems, they are typically neglected in the actual control design, i.e., their insights are used to design a controller by hand but not explicitly used in the optimization. The second part of the paper therefore addresses the problem of how to incorporate the developed noise budget in the optimization of K_{RFC}.

3. System modeling

The first step in developing the noise budget is to model the dynamics of the system into a block diagram, from which the relations between the external inputs and output variable can be computed such that the external inputs can be projected onto the output. To this end, the resonance condition is first rewritten such that it can be modeled in a block diagram. The block diagram of the control scheme is then presented as well as the derivation of the models for each block.

3.1. Block diagram of control scheme

The main reason for using a block diagram to model the system is that it allows the computation of the closed-loop relation between input and output as rational transfer functions and subsequently the computation of the individual contributions of the input to the output in the frequency domain, i.e., producing a noise budget. The block diagram and its closed-loop relations will furthermore also be used in the controller synthesis in Section 5.

In Fig. 1(b) the block diagram of the control scheme for CARM and laser frequency stabilization is visualized. The three dash-dotted rectangular boxes correspond to the same colored boxes as in Fig. 1(a) and represent the three nested control loops: the PS loop (orange), the SSFS loop (blue) and RFC loop (green). Each block represents a linear dynamic system, where the purple blocks represent controllers, the yellow blocks represent mechanical transfer functions and the red blocks represent optical transfer functions. The signals $P_\bullet$ are the error signals in Watts, $\delta\nu_\bullet$ the fluctuations of the laser frequency in Hertz, $\delta x_\bullet$ the changes in cavity length in meters and $u_\bullet$ the control signals in Volts. The output of the control system is $\delta\nu_C$, which is the laser frequency circulating in the arm cavities. The system is furthermore subject to a set of disturbances, represented by the external signals, each of which is investigated in Section 4.1. An overview of the variables used in the block diagram is given in Table 1.

An important property of the model is the incorporation of the resonance condition for the arm cavities as well as the IMC cavity since both their lengths and the laser frequency are actively controlled and these cavities require to be on resonance. The resonance condition is defined in (3) as the difference between the length of the cavity and the wavelength. This relation cannot be directly used since we control the laser frequency rather than its wavelength and we furthermore require a relation in terms of a difference between variables (i.e., a summation) rather than a ratio.

3.2. Modeling resonance condition

The objective of this section is to find an equation defining the resonance condition as a difference between the cavity length and the laser frequency circulating in this cavity. Controlling the laser frequency is equivalent to controlling the wavelength since

$$c = \lambda \cdot \nu, \tag{4}$$

where c is the speed of light, λ the laser wavelength and ν the laser frequency in Hz. Assuming small fluctuations, the derivative of (3) yields

$$\frac{\delta\lambda}{\lambda_0} = \frac{\delta x}{x_0}, \tag{5}$$

with $\lambda_0 = 1064\,\text{nm}$ the nominal laser wavelength, x_0 the nominal cavity length and δx, $\delta\lambda$ the fluctuations of the cavity length and wavelength respectively. The derivative of (4) yields

$$\frac{\delta\lambda}{\lambda_0} = -\frac{\delta\nu}{\nu_0}, \tag{6}$$

with ν_0 the nominal laser frequency and $\delta\nu$ the fluctuations around this nominal value. Combining (4), (5) and (6) then gives

$$\delta\nu + \frac{c}{\lambda_0 x_0}\delta x = \delta\nu - \gamma(x_0)\delta x = \delta\nu - \delta\nu^{res} = 0, \tag{7}$$

with

$$\gamma(x_0) = -\frac{c}{\lambda_0 x_0}, \tag{8}$$

and

$$\delta\nu^{res} = \gamma(x_0)\delta x. \tag{9}$$

Eq. (7) can be interpreted as the cavity having a resonance frequency, which is a function of the scaling factor $\gamma(x_0)$ and the fluctuations around the nominal length of the cavity. The cavity is then on resonance when the difference between the cavity resonance frequency and laser frequency is zero.

In the control scheme, both the arm cavities and IMC cavity have their length and circulating laser frequency controlled. The resonance condition for the arm cavities is defined in the block diagram by the relation

$$\delta\nu_C - \delta\nu_C^{res} = \delta\nu_C - \beta\delta x_C, \tag{10}$$

where according to (8) $\beta = \gamma(3000)$ since the cavity is 3 km long. The IMC cavity resonance condition is defined by the difference equation

$$\delta\nu_{MC} - \delta\nu_{MC}^{res} = \delta\nu_{MC} - \alpha\delta x_{MC}, \tag{11}$$

with $\alpha = \gamma(144)$, since the IMC cavity is 144 m long.

3.3. Derivation of models for blocks

Each block in the block diagram is modeled as a rational transfer function (or a simple gain) which will later allow to compute closed-

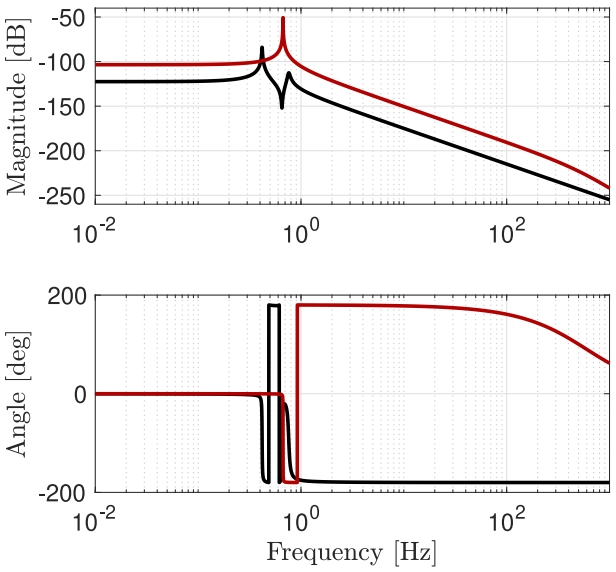

Fig. 2. Bode plot of the mechanical transfer function A_{MC} (—) and A_{C} (—). The transfer functions are modeled as harmonic oscillators representing the suspension dynamics and an additional pole pair is used to model the actuator dynamics.

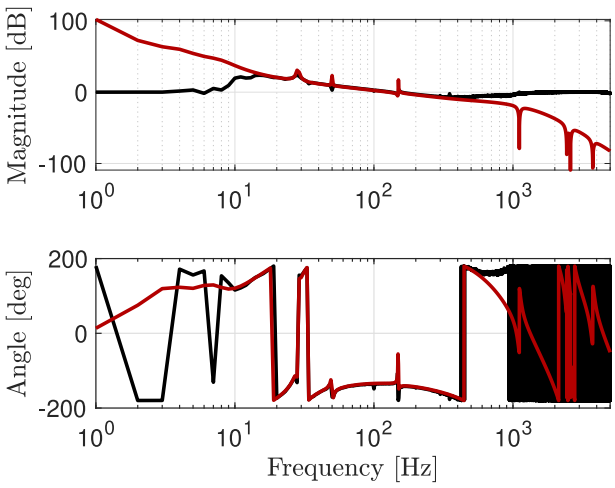

Fig. 3. Comparison between the modeled (—) and measured (—) FRF of the open-loop system in (12), measured on AdV+. The FRF is used to identify the optical gain of G_{RFC} and to verify whether the overall dynamics between the model and measurement match. After adjusting the optical gain of G_{RFC}, the modeled and measured FRF match well.

loop contributions of each noise source to the output in the frequency domain. The gray triangular blocks α and β have already been derived in Section 3.2. The yellow blocks are the mechanical transfer functions and their models are based on internal models already available at AdV+. The mechanical transfer function A_{I} for the laser is modeled as a gain and the transfer functions A_{MC}, A_{C} are modeled as harmonic oscillators relating the voltage sent to the actuators to a motion of the mirrors. The Bode plot of these transfer functions is depicted in Fig. 2. Note that for A_{MC} an additional pole-pair is present at 300 Hz representing the actuator dynamics, while the harmonic oscillator represents the dynamics of the suspension system translating a force on the mirror to the corresponding mirror motion. The DC gains used in the models are obtained through experiments on the detector and are $0.75\,\mu\mathrm{m\,V^{-1}}$ for A_{C} and $6.7\,\mu\mathrm{m\,V^{-1}}$ for A_{MC}.

The optical transfer functions consist of only a single pole, i.e., the cavity pole, which is known in AdV+ from simulations or measurements. Their DC gain, also known as the optical gain in $\mathrm{W\,Hz^{-1}}$, is also of importance since this enables calibration of the error signals. It is however difficult to obtain these from simulations since these simulations do not include the imperfections of the interferometer, which the DC gain is very dependent on.

Instead, the optical gains of the three blocks G_{C}, G_{RFC} and G^r_{MC} are experimentally determined using two dedicated measurements. Note that the optical gain of G^t_{MC} is $1\,\mathrm{Hz\,Hz^{-1}}$ since it is a transmission transfer function only containing the cavity pole. For the first measurement, a simplified control configuration is used, where the RFC error signal is directly used to actuate on the IMC mirror and the arm cavities are left uncontrolled. Using this configuration (for which a block diagram is omitted for brevity), the Frequency Response Function (FRF) of the open-loop transfer function is measured by injecting bandpass-filtered white noise and compared to the FRF of the model. The open-loop transfer function for this configuration is given by

$$\frac{P_{\mathrm{RFC}}(s)}{e_{\mathrm{RFC}}(s)} = \frac{A_{\mathrm{I}}K_{\mathrm{PS}}G^r_{\mathrm{MC}}}{1+A_{\mathrm{I}}K_{\mathrm{PS}}G^r_{\mathrm{MC}}}\cdot \alpha A_{\mathrm{MC}}K_{\mathrm{MC}}G_{\mathrm{RFC}}G^t_{\mathrm{MC}} \approx \alpha A_{\mathrm{MC}}K_{\mathrm{MC}}G_{\mathrm{RFC}}G^t_{\mathrm{MC}}, \tag{12}$$

with $P_{\mathrm{RFC}}(s) = \mathcal{L}\{P_{\mathrm{RFC}}(t)\}$ and $e_{\mathrm{RFC}}(s) = \mathcal{L}\{e_{\mathrm{RFC}}(t)\}$ the Laplace transforms of their respective time domain signals and the last equality furthermore holds since

$$\frac{A_{\mathrm{I}}K_{\mathrm{PS}}G^r_{\mathrm{MC}}}{1+A_{\mathrm{I}}K_{\mathrm{PS}}G^r_{\mathrm{MC}}} \approx 1\;\forall\,\omega \ll 2\pi 110\,\mathrm{kHz}, \tag{13}$$

because the UGF of the PS loop is at 110 kHz and $\left|A_{\mathrm{I}}K_{\mathrm{PS}}G^r_{\mathrm{MC}}\right| \gg 1$ below this frequency. The only unknown gain in the last equality of (12) is the optical gain of G_{RFC}, which is determined by correcting its value such that the model and measurement of (12) match. A comparison of the model and measured FRF is shown in Fig. 3, where the optical gain of G_{RFC} is determined using the aforementioned procedure. The model and measurement are in good correspondence between 10 and 500 Hz. The discrepancies outside this frequency range stem from the fact that band-limited white noise has been injected in the aforementioned frequency range and the FRF is computed by directly computing (12), which is 1 at frequencies where the injected noise is zero.

The optical gains of G^r_{MC} and G_{C} are determined by matching the FRF of the modeled and measured open-loop transfer function of the SSFS (the blue + orange system in Fig. 1(b)). This open-loop is given by

$$\frac{P_{\mathrm{C}}}{e_{\mathrm{C}}} = G_{\mathrm{C}}G^t_{\mathrm{MC}}S_{\mathrm{PS}}F_{\mathrm{I}}K_{\mathrm{PS}}\left(K_{\mathrm{SSFS}} + G^r_{\mathrm{MC}}\alpha A_{\mathrm{MC}}K_{\mathrm{MC}}\right) = G_{\mathrm{C}}G^t_{\mathrm{MC}}\left(S_{\mathrm{PS}}F_{\mathrm{I}}K_{\mathrm{PS}}K_{\mathrm{SSFS}} + T_{\mathrm{PS}}\alpha A_{\mathrm{MC}}K_{\mathrm{MC}}\right), \tag{14}$$

with

$$S_{\mathrm{PS}} = \frac{1}{1+F_{\mathrm{I}}K_{\mathrm{PS}}G^r_{\mathrm{MC}}},\quad T_{\mathrm{PS}} = 1 - S_{\mathrm{PS}}. \tag{15}$$

As mentioned in Section 2.2, the SSFS loop uses two different control paths to lock the laser on the arm cavities, at low frequencies by controlling the IMC length and at high frequencies by acting on the setpoint of the PS loop. These two control paths are represented in (14) by the two terms in between the brackets. Below a certain frequency, the gain of the K_{MC} path is high and the gain of K_{SSFS} is low and above this frequency the opposite holds. The ratio in terms of gain between the two determines the crossover frequency and therefore also the shape of the open-loop FRF. Note that only G^r_{MC} is present in the term in between the brackets in the first equality and the optical gain of G^r_{MC} can thus be adjusted until the modeled and identified FRF match in terms of shape. The optical gain of G_{C} is then obtained by shifting the modeled FRF up or down until the gains of the modeled and measured FRF match. This procedure is applied to find the gains of G^r_{MC} and G_{C} using the FRFs presented in Fig. 4. The modeled and identified dynamics match well in the identified frequency range, albeit with small discrepancies in the phase which have only a limited effect on the resulting noise budget.

Using these procedures, the optical gains as noted in Table 2 are found and all blocks are modeled and experimentally verified.

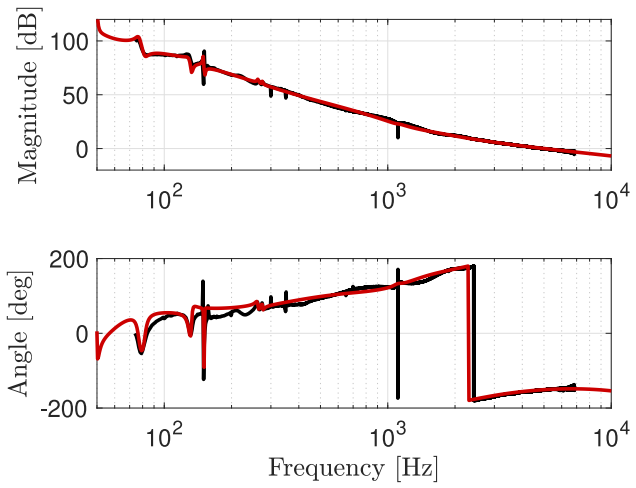

Fig. 4. Comparison between the modeled (—) and measured (—) FRF of the open-loop system in (14), measured on AdV+. The FRF is used to identify the optical gains of G^r_{MC} and G_{C} and to verify whether the overall dynamics between the model and measurement match. After adjusting the optical gains of G^r_{MC} and G_{C}, the modeled and measured FRF match well.

Table 2
The optical gains of the optical transfer functions as measured on AdV+.

Optical transfer function	Optical gain
G_{C}	$0.033\,\mathrm{W\,Hz^{-1}}$
G_{MC}	$4.12\times10^{-5}\,\mathrm{W\,Hz^{-1}}$
G_{RFC}	$1.52\times10^{-8}\,\mathrm{W\,Hz^{-1}}$

4. Noise budget

For this noise budget, two critical assumptions are made. The first assumption is that the system is Linear Time-Invariant. The linearity assumption is valid since the system behaves predominantly linear due to its static operating point. The time-invariance assumption does not necessarily hold in practice since the optical response varies over time due to thermal transients as well as changes in the alignment of the optics. These fluctuations are however assumed to be sufficiently small compared such that they do not significantly affect the noise budget. The second assumption is that all noises are stationary, which for almost all noises holds. This is observed through the stationary behavior of the sensitivity, which would otherwise also fluctuate as a result of the non-stationary behavior of the noises. The non-stationary assumption is however not true for seismic noise. The assumption is nevertheless made that the non-stationary behavior is sufficiently small such that this does not influence the noise budget in the sense that for each frequency the limiting noise can still be confidently identified in the noise budget.

In the first part, the derivation of the models for the different disturbances as well as the closed-loop equations from the disturbances to the laser frequency fluctuations are presented. Then, the noise budget is presented and experimentally validated using the measured frequency fluctuations on AdV+.

4.1. Modeling disturbances

There are many disturbances affecting the different loops through different disturbance paths. A conscious choice has been made to model only a subset of these disturbances, which from experience are expected to be the most limiting. This choice follows from the objective of the noise budget in this paper, which is to characterize the system and optimize the controller rather than to use it in the design phase of the detector. For this objective, a noise budget that models only the limiting disturbances at each frequency is sufficient. The presented framework to derive the noise budget can however readily be used to include more disturbances, given that the disturbance models and the location at which they enter the loops are known.

The disturbances are modeled as filtered white noise, i.e.,

$$\mathcal{P}(w_i) = \left|H_i(j\omega)\right|^2 \cdot \mathcal{P}(\epsilon), \tag{16}$$

with $\mathcal{P}(\cdot)$ the Power Spectral Density (PSD) of a disturbance, $H_i(j\omega)$ the transfer function that colors the noise and ϵ unit-power white noise. All disturbances are grouped in a single vector w

$$w = \begin{bmatrix} d_l & \eta_{\mathrm{MC}} & d_{\mathrm{MC}} & \eta_{\mathrm{C}} & d_{\mathrm{C}} & \eta_{\mathrm{RFC}} \end{bmatrix}^T, \tag{17}$$

where $\eta_{\bullet}$ are noises for the respective sensors of each loop, d_{C}, d_{MC} represent seismic noise affecting the cavity lengths and d_{l} represents the free running laser frequency fluctuations. The derivations of these noise models are addressed next.

4.1.1. Sensor noise

For AdV+, the photodiodes are typically limited by shot noise, which is why only this sensor noise is modeled for the PS and SSFS loop. The shot noise is frequency independent and is computed according to Cahillane and Mansell [16]

$$\mathcal{P}(\eta^{\mathrm{shot}}) = \sqrt{\frac{hc\,P_{DC}}{n\lambda}} \left[\frac{\mathrm{W}}{\sqrt{\mathrm{Hz}}}\right], \tag{18}$$

with $h = 6.626\times10^{-34}\,\mathrm{J\,Hz^{-1}}$ being the Planck constant, P_{DC} the DC power on the respective photodiode, n the quantum efficiency of the photodiode (which is assumed to be 0.95) and λ the wavelength of the laser. For all three sensors, the shot noise is computed by using the DC power measured when the interferometer is in its final operating state. The DC powers used in the noise budget for the photodiodes are 49 mW for the B4 photodiode used for the SSFS loop, 630 mW for the IMC photodiode and 200 mW for the RFC photodiode.

4.1.2. RFC thermal noise

The RFC, used to estimate the laser frequency fluctuations, is subject to thermal effects that translate into length fluctuations. This is considered to be a sensor noise and is modeled as [5,17]

$$\mathcal{P}(\eta^{\mathrm{length}}_{\mathrm{RFC}}) = \frac{0.1}{\sqrt{f}} \left[\frac{\mathrm{Hz}}{\sqrt{\mathrm{Hz}}}\right]. \tag{19}$$

This noise is additionally incorporated for η_{RFC} as it will show to be a dominant disturbance.

4.1.3. Seismic noise

The mirrors in AdV+ are isolated from ground motion by large suspension systems that use an actively controlled Inverted Pendulum followed by a chain of pendula to provide attenuation at 10 Hz of more than 10 orders of magnitude [18]. The effect of seismic noise on the mirrors is modeled as a product of two terms, i.e.,

$$\mathcal{P}(d_{\bullet}) = X_{\mathrm{mir}}(\omega) = \left|X_{\mathrm{susp}}(j\omega)\right| \cdot X_{\mathrm{ground}}(\omega), \tag{20}$$

where the first term in the last equality represents the suspension dynamics and the second term represents the seismic motion. The suspension dynamics are modeled as the product of M damped harmonic oscillators

$$X_{\mathrm{susp}}(j\omega) = \prod_{i=1}^{M} \frac{\psi_i^2}{(j\omega)^2 + 2\zeta_i\psi_i j\omega + \psi_i^2}, \tag{21}$$

in which ψ_i represents the eigenfrequency and ζ_i the damping factor of the respective harmonic oscillator. A damped harmonic oscillator is chosen here since feedback control is used in the suspensions to damp the typically lowly damped suspension modes. For the noise model of the arm cavities d_{C} $M = 7$ is used and for the IMC noise model d_{MC}

$M = 5$ is used. The suspension frequencies ψ_i are placed between 0.07 and 2 Hz since they are known to be in this frequency range.

The seismic noise is estimated using measured percentile ground spectra at the AdV+ site [19], which is approximated by

$$X_{\text{ground}}(\omega) = \frac{2 \cdot 10^{-6}}{\omega^2}. \tag{22}$$

An important simplification made here is that the length fluctuations of a single cavity are modeled here by the motion of a single mirror, while in practice the cavity length fluctuations are a function of the combined relative motion of the cavity mirrors. Modeling the combined stochastic effect of ground motion on a cavity is complicated, but, as it will be experimentally shown in Section 4.3, the assumption of a single mirror model proves to be sufficiently accurate to describe the dominant dynamics.

4.1.4. Laser frequency fluctuations

The frequency fluctuations of the uncontrolled laser are obtained from the specification sheet of the supplier and are given by

$$\mathcal{P}(d_l) = 10^4 \cdot f \left[\frac{\text{Hz}}{\sqrt{\text{Hz}}}\right]. \tag{23}$$

4.2. Derivation of projection equations

The next step is to derive the projection equations, i.e., the closed-loop transfer functions from the disturbances w to the output of the system $\delta\nu_C$. These equations are derived using the block diagram in Fig. 1(b) and are given by

$$\begin{aligned}
\mathcal{P}(\delta\nu_C) = &\left|G^t_{MC} S_{RFC} S_{PS}\right|^2 \cdot \mathcal{P}(d_l) \\
&+ \left|G^t_{MC} S_{RFC} S_{PS} A_l K_{PS}\right|^2 \cdot \mathcal{P}(\eta_{MC}) \\
&+ \left|G^t_{MC} S_{RFC} S_{PS} A_l K_{PS} G^r_{MC} \alpha\right|^2 \cdot \mathcal{P}(d_{MC}) \\
&+ \left|G^t_{MC} S_{RFC} \mathcal{G}\right|^2 \cdot \mathcal{P}(\eta_C) \\
&+ \left|G^t_{MC} S_{RFC} \mathcal{G} G_C \beta\right|^2 \cdot \mathcal{P}(d_C) \\
&+ \left|G^t_{MC} S_{RFC} \mathcal{G} G_C \beta A_C K_{RFC}\right|^2 \cdot \mathcal{P}(\eta_{RFC}),
\end{aligned} \tag{24}$$

with

$$\begin{aligned}
S_{RFC} = &(1 + S_{PS} A_l K_{PS} \left(K_{SSFS} + G^r_{MC} \alpha A_{MC} K_{MC}\right) \\
&G_C (1 + \beta A_C K_{RFC} G_{RFC}) G^t_{MC})^{-1},
\end{aligned} \tag{25}$$

and

$$\mathcal{G} = S_{PS} A_l K_{PS} (K_{SSFS} + G^r_{MC} \alpha A_{MC} K_{MC}). \tag{26}$$

Using (24) with the models of the disturbances derived in Section 4.1 then yields the closed-loop contribution of each noise source to the laser frequency fluctuations.

4.3. Noise budget for laser frequency fluctuations

In Fig. 5, the noise budget for the laser frequency fluctuations is depicted. It combines the frequency domain models of the disturbances as derived in Section 4.1 with the projection equations of Section 4.2 to obtain the closed-loop contribution of each disturbance w to the output $\delta\nu_C$ in the frequency domain. The sum of all the disturbances, i.e., the expected spectrum of $\delta\nu_C$ based on the modeled disturbances, is represented by the gray dash-dotted line.

To verify the noise budget, a measurement of $\delta\nu_C$ is also shown. There is no sensor available in AdV+ that directly measures $\delta\nu_C$ so the RFC sensor is used instead to obtain a measured reconstruction of $\delta\nu_C$. This measured reconstruction is obtained through

$$\delta\hat{\nu}_C = G^{-1}_{RFC} \hat{e}_{RFC}, \tag{27}$$

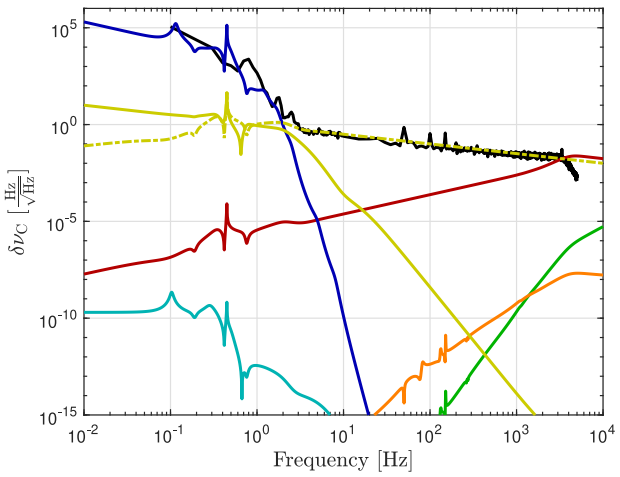

Fig. 5. Noise budget for the control system of CARM with (—) measurement of $\delta\nu_C$; (—) η_C; (—) d_l; (—) d_C; (—) d_{MC}; (—) η_{MC}; (—) η_{RFC} in-loop; (- - -) η_{RFC} out-of-loop; (- · - · -) sum of disturbances w. The seismic noise d_C is dominating the RMS through its low frequency contribution.

where $\hat{e}_{RFC}$ is the measurement of the RFC photodiode obtained from AdV+, G_{RFC} the model of the RFC optical response as found in Section 3.3 and $\delta\hat{\nu}_C$ the estimate of the laser frequency based on the measurements.

Using the RFC sensor to obtain the reconstructed laser frequency fluctuations has an important consequence. The projection equations in Section 4.2 are all computed from w to $\delta\nu_C$, while the plot shows $\hat{e}_{RFC}$, which is the only frequency noise witness available. Computing the closed-loop equations from w to e_{RFC} and using (27) to obtain the closed-loop transfer function from w to $\delta\nu_C$ will yield (24) for all disturbances w, except for η_{RFC}. From (24) the coupling from η_{RFC} to $\delta\nu_C$ is

$$\frac{\delta\nu_C}{\eta_{RFC}} = G^t_{MC} S_{RFC} \mathcal{G} G_C \beta A_C K_{RFC} = S_{RFC} L_{RFC} G^{-1}_{RFC} = T_{RFC} G^{-1}_{RFC}, \tag{28}$$

where L_{RFC} is the open-loop transfer function of the complete control system and where T_{RFC} denotes the complementary sensitivity, i.e.,

$$T_{RFC} = \frac{L_{RFC}}{1 + L_{RFC}} = 1 - S_{RFC}. \tag{29}$$

Computing the coupling from η_{RFC} to e_{RFC} yields

$$\frac{e_{RFC}}{\eta_{RFC}} = S_{RFC}, \tag{30}$$

which is different from the coupling of η_{RFC} to $\delta\nu_C$ as in (28). This difference in coupling is a consequence of using an in-loop error signal (a feedback loop is closed on this error signal). The coupling of η_{RFC} to the true $\delta\nu_C$ and the reconstructed measurement are therefore plotted in Fig. 5, where the dashed yellow line is the coupling of η_{RFC} to the used error signal $\hat{e}_{RFC}$, i.e., the in-loop contribution of η_{RFC} as formulated in (30), and the thick yellow line is the contribution of η_{RFC} to the true laser frequency fluctuations based on (28) (and thus also (24)).

Comparing the measured $\delta\nu_C$ (black line) to the modeled contributions shows that the system is completely understood at all frequencies in terms of the limiting disturbances. The noise budget furthermore shows that η_{RFC} limits the spectrum between 4 Hz and 5 kHz, but this is thus an artifact of how the estimate of the laser frequency fluctuations are obtained on the system since a sufficiently sensitive out-of-loop sensor is not available. In fact, η_{RFC} is only expected to be limiting between 4 and 20 Hz, above which the shot noise of the arm cavity photodiode will limit the spectrum. Below 4 Hz, the seismic noise coupling to the arm cavity mirrors is limiting the laser frequency fluctuations and this is also limiting the total RMS of $\delta\nu_C$, which is expected considering the lack of attenuation of seismic motion below 10 Hz.

5. $\mathcal{H}_2$-based controller design

The noise budget shows that the RMS of $\delta\nu_C$ is dominated by seismic noise coupling to the arm cavity mirrors. To minimize the RMS, the RFC controller is re-tuned since this controller is the only one with which the seismic motion-induced laser frequency fluctuations can be attenuated. In this section, a systematic design procedure is presented that uses the noise budget to synthesize a norm optimal controller for K_{RFC}. First, a background on $\mathcal{H}_2$ optimal control is given, after which the plant used for synthesis is derived. Finally, an $\mathcal{H}_2$ optimal controller is synthesized and a manual control design based on the $\mathcal{H}_2$ optimal controller is presented.

5.1. Control objectives

It has been noted in Section 2 that the main objective of K_{RFC} is to minimize the RMS of $\delta\nu_C$. If that were the sole design objective then any type of controller optimization would give a controller with the highest attainable UGF. The coupling to DARM is however also of critical importance since the DARM spectrum directly determines the sensitivity of the detector. For the RFC loop, the actuators on the end mirrors are used, which send a common voltage to both mirrors. Small imbalances between the actuator gains will directly induce a motion in DARM, since this is the difference in length between the two arms (and thus directly influenced by differential end mirror motions). The coupling from the RFC loop to DARM is written as

$$x_{C\to D} = A_C \cdot \rho \cdot u_{RFC}, \tag{31}$$

where $x_{C\to D}$ is DARM motion resulting from the actuation on the end mirrors of the RFC loop and $\rho \in \mathbb{R}$ is a constant coupling factor. Based on past experiences, a worst-case $\rho = 0.01$ is chosen, which equals 1 percent of coupling between CARM and DARM. Since Gravitational Waves are detected above 10 Hz, the goal is to minimize $x_{C\to D}$ above this frequency, which is equivalent to minimizing the actuation signal u_{RFC} above 10 Hz.

The controller synthesis thus requires finding the optimal controller that minimizes $\delta\nu_C$ while keeping the spectral contributions of u_{RFC} above 10 Hz under a certain bound. Note that the exact bound for u_{RFC} is not yet known so the controller design requires an iterative procedure between the implementation of a synthesized controller and its update, depending on whether the bounds on u_{RFC} are met.

5.2. Controller synthesis using the $\mathcal{H}_2$ norm

Controller design for control loops in a Gravitational Wave detector is typically a complex and time-consuming endeavor due to the stringent RMS requirements combined with a variety of disturbances, some of which vary over time. Structured design methods for these controllers are thus desired, where ideally the controller is synthesized based on some system-based design criterion. The approach taken in this paper is therefore to synthesize a $\mathcal{H}_2$ norm optimal controller, which, as it will be shown later in this section, minimizes the RMS of the output which is our design objective.

The drawback of this approach is two-fold. First, it is not possible to incorporate the time-varying behavior in the optimization, leading to a controller that is not necessarily optimal for all time instances. An example is the seismic motion, where a simple model is used in (22), which for example does not model the microseismic peaks [20] that vary as a function of the weather. Second, a $\mathcal{H}_2$ synthesized controller has no guarantees on stability margins [21], meaning the margins can be arbitrarily small. The approach taken in this paper is therefore to use $\mathcal{H}_2$ synthesis on a nominal model and to derive a manual feedback controller based on the $\mathcal{H}_2$ synthesized controller. The proposed approach allows to quickly iterate on the control design and simultaneously incorporate knowledge of the time-varying effects as well as sufficient stability margins in the design.

The first step for the controller synthesis is to formulate the control problem in the generalized plant form, i.e., formulate the plant P such that

$$\begin{bmatrix} z \\ y \end{bmatrix} = P \begin{bmatrix} w \\ u \end{bmatrix}, \tag{32}$$

where w are the external disturbances, z the outputs to be minimized and u, y the respective inputs and outputs of the controller blocks that are to be synthesized. The $\mathcal{H}_2$ synthesis then minimizes [22]

$$\|F(s)\|_2 = \sqrt{\frac{1}{2\pi}\int_{-\infty}^{\infty} \mathrm{tr}(F(j\omega)F(j\omega)^H)d\omega}, \tag{33}$$

where $F(s)$ is the closed-loop function

$$F(s) : w \to z. \tag{34}$$

When the inputs w are unit-power white noise, minimization of the $\mathcal{H}_2$ norm of $F(s)$ then minimizes the RMS of z [22].

5.3. Formulating the generalized plant

This section presents the steps to formulate the generalized plant P for this particular control problem. Based on the block diagram of Fig. 1(b), the relation between the inputs and outputs for the generalized plant is determined. Rather than using the complete block diagram, the input–output relation can be reduced to a few blocks under the assumption that the PS and SSFS loop are closed with a significantly higher UGF than the RFC loop. The advantage of this reduction in blocks is that it greatly reduces the computational complexity. Since the PS and SSFS loop are closed with UGFs of respectively 7 kHz and 110 kHz, this assumption holds. Computing the transfer function from u_{RFC} to e_{RFC} then gives

$$\frac{e_{RFC}}{u_{RFC}} = Q_{RFC}^{eq} = G_C G_{RFC} S_{SSFS} G_{MC}^t S_{PS} A_l K_{PS} (K_{SSFS} + G_{MC}^r \alpha A_{MC} K_{MC}) \beta A_C, \tag{35}$$

with

$$S_{SSFS} = \left(1 + G_C G_{MC}^t S_{PS} A_l K_{PS} \left(K_{SSFS} + G_{MC}^r \alpha A_{MC} K_{MC}\right)\right)^{-1}. \tag{36}$$

Eq. (35) is rewritten to

$$Q_{RFC}^{eq} = \beta G_{RFC} A_C T_{SSFS} \approx \beta G_{RFC} A_C \tag{37}$$

since

$$T_{SSFS}(j\omega) = 1 - S_{SSFS}(j\omega) \approx 1 \;\forall\; \omega \ll 2\pi 7\,\mathrm{kHz}. \tag{38}$$

Only the blocks β, G_{RFC} and A_C are therefore required in the synthesis.

The next step is to define the inputs and outputs of the generalized plant. The control variables u, y are respectively the output and input of the controller K_{RFC}. For the external disturbances w, only the disturbances d_C and η_{RFC} are required from the noise budget since these disturbances are limiting the spectrum while the coupling of third limiting disturbance η_C is not influenced by a change of K_{RFC}. For the performance variable z, the laser frequency fluctuations $\delta\nu_C$ is chosen since the goal is to minimize its RMS. Additionally, as noted in Section 5.1, the coupling to DARM should be kept under a certain frequency-dependent threshold so the correction signal u_{RFC} is also used as a performance variable z that has to be minimized and this variable is denoted by u_{RFC}^z.

Using the defined inputs and outputs for the generalized plant, the generalized plant itself is formulated as

$$\begin{bmatrix} \delta\nu_C \\ u_{RFC}^z \\ e_{RFC} \end{bmatrix} = \underbrace{\begin{bmatrix} \beta & 0 & \beta A_C \\ 0 & 0 & 1 \\ -G_{RFC}\beta & -1 & -G_{RFC}\beta A_C \end{bmatrix}}_{=P} \begin{bmatrix} d_C \\ \eta_{RFC} \\ u_{RFC} \end{bmatrix}. \tag{39}$$

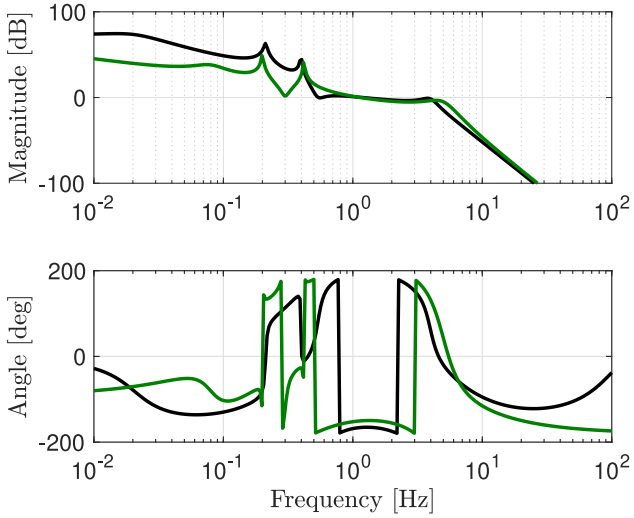

Fig. 6. Bode plot of the $\mathcal{H}_2$ synthesized controller (—) and the controller manually designed based on the $\mathcal{H}_2$ optimal controller for K_{RFC} (—) The manually tuned controller has significantly larger stability margins, at the expense of some low frequency gain and high frequency roll-off.

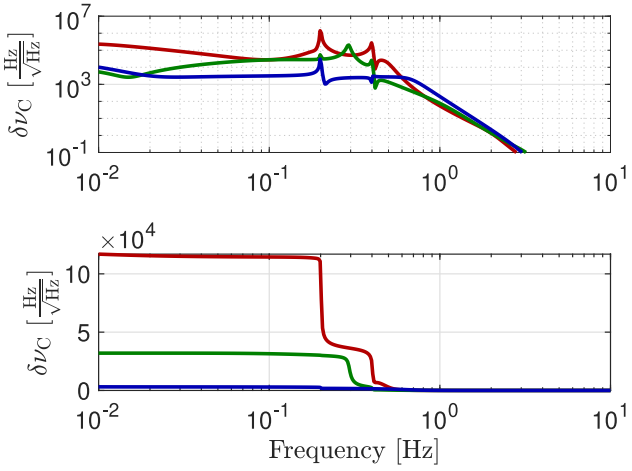

Fig. 7. Simulated laser frequency fluctuations with (—) original controller, (—) $\mathcal{H}_2$ based manually tuned controller and (—) $\mathcal{H}_2$ synthesized controller. Top plot: Auto spectral density; Bottom plot: Cumulative PSD integrated from 1 kHz to DC.

The final step is to introduce the weighting filters that determine the relative weighting of each input and output in the optimization. The weighting filters are defined as

$$\tilde{P} = W \cdot P \cdot V, \tag{40}$$

where $\tilde{P}$ is the weighted generalized plant and W, V are the input and output weightings respectively. For the input weighting, the noise models derived in Section 4.1 are used, i.e.,

$$W = \mathrm{diag}([H_{d_C}\ H_{\eta_{\mathrm{RFC}}}\ 1]). \tag{41}$$

For the output weighting, a frequency-dependent weighting filter on the correction signal u_{RFC} is used, which enforces roll-off of the correction signal above a certain frequency and therefore minimizes the coupling to DARM. This weighting filter H_u is defined as the inverse of an N order lowpass filter with its cut-off frequency at 3 Hz to enforce sufficient roll-off above 10 Hz and obtain a UGF of at most 2 Hz. The output weighting filter is defined as

$$V = \mathrm{diag}([\kappa\ H_u\ 1]), \tag{42}$$

where $\kappa \in \mathbb{R}$ is used to scale the relative weighting of the RMS suppression of $\delta\nu_C$ with respect to the correction signal u_{RFC}.

The optimal controller $K_{\mathrm{RFC}}^{\mathrm{opt}}$ is then found by solving

$$K_{\mathrm{RFC}}^{\mathrm{opt}} = \arg\min_{K_{\mathrm{RFC}}} = \|\mathcal{F}_l(\tilde{P},\ K_{\mathrm{RFC}})\|_2, \tag{43}$$

where $\mathcal{F}_l$ denotes the left Linear Fractional Transformation [22]. The solution to this optimization problem follows from two Riccati equations [23].

5.4. Control design based on optimization

The control objectives as well as the optimization criterion have now been defined. Since there is no hard criterion on the output spectrum u_{RFC}, the synthesis requires the manual tuning of the output weighting filter V until a satisfactory trade-off between the RMS error of $\delta\nu_C$ and the control effort u_{RFC} above 10 Hz is found. Eq. (43) is thus iteratively solved with different weighting until a satisfactory trade-off is found. For the final optimization, a fourth-order lowpass filter is used and $\kappa = 2 \cdot 10^{-4}$.

A manual controller is then tuned based on the synthesized controller to deal with the time-varying seismic disturbance as well as the lack of stability margins. A comparison of the two controllers is shown in Fig. 6. The synthesized controller is shown to have very low stability margins as the phase margin is roughly 10 degrees. The manual control design therefore takes the synthesized controller as a baseline and two adjustments are made to obtain a 6 dB modulus margin, i.e., a maximum of 6 dB peak in the sensitivity function, which guarantees a sufficient stability margin. The first change is the shift of the two zeros from 0.5 to 0.3 Hz since the seismic motion is overestimated in (22) with respect to a typical measured seismic spectrum. Second, the poles at 4 Hz are shifted to 5 Hz, which increases the stability margin at the expense of the roll-off. This is nevertheless not expected to be a problem considering a worst case scenario was taken for the coupling to DARM. With these two changes, a controller with a 6 dB modulus margin is obtained that maintains the structure of the synthesized $\mathcal{H}_2$ optimal controller.

In Fig. 7 the simulated laser frequency fluctuations $\delta\nu_C$ for the different controllers are compared. An optimal control design leads to a flat spectrum, which the synthesized controller indeed produces. The manually tuned controller has significantly less performance due to the required changes improving the stability margins. It has however increased performance in the 0.1 to 0.7 Hz range where the majority of the RMS motion comes from. An expected improvement of roughly a factor 3 in RMS is therefore simulated for the new controller with respect to the original controller. This number may however vary in practice due to the time-varying behavior of the seismic motion. Note furthermore that the new controller, aside from the 0.3 Hz due to overestimation of ground motion in the model, provides a flatter error spectrum compared to the original controller, which indicates a more optimal control performance.

6. Experimental results

Experimental results of the designed controller on AdV+ are presented in this section to evaluate its performance compared to the original controller. The coupling to DARM is also measured to determine whether the new controller achieves the roll-off requirements.

6.1. Controller performance

The new K_{RFC} controller derived in Section 5.4 is implemented in AdV+ to compare its performance with the original controller. In Fig. 8, measurements of $\delta\nu_C$ for the two controllers from AdV+ are depicted. A measurement of the signal e_{RFC}, calibrated in Hertz using the estimate of G_{RFC}, is again used to obtain an estimate of $\delta\nu_C$ at low frequencies.

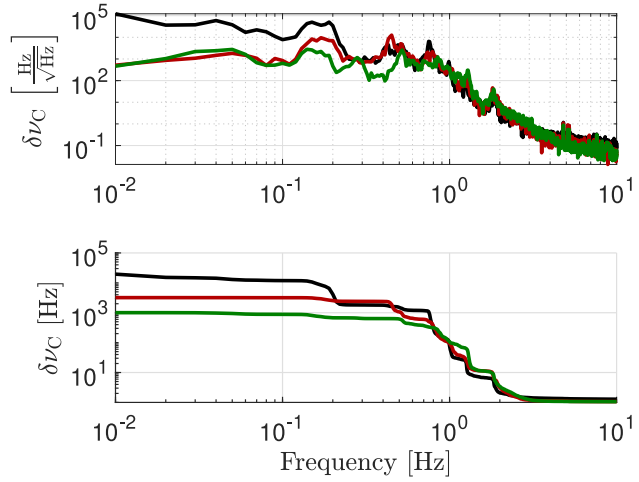

Fig. 8. Measured laser frequency fluctuations on AdV+ with (▬) controller off, (▬) original controller, (▬) $\mathcal{H}_2$ based controller. Top plot: Auto spectral density; Bottom plot: Cumulative PSD integrated from 5 kHz to DC. The new controller achieves roughly a factor 3 better RMS and improves the attenuation in the 0.1 to 0.7 Hz range.

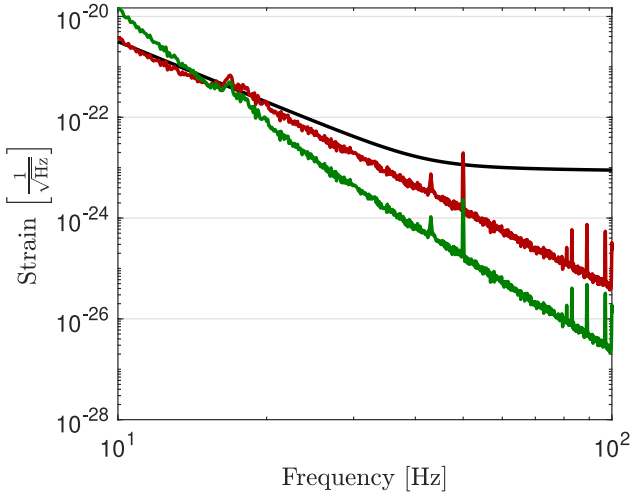

Fig. 9. Measured coupling of CARM noise onto the sensitivity of AdV+. (▬) target sensitivity for O4 science run; (▬) projection of CARM noise using the original controller; (▬) projection of CARM noise using the $\mathcal{H}_2$ based controller.

The top plot shows the Auto Spectral Density (ASD) of $\delta\nu_C$. The new controller reduces the ASD by roughly a factor 3 between 0.1 and 0.7 Hz and the spectrum is indeed more flat compared to the original controller. There are however still several peaks visible in the 0.1 and 1 Hz range, which is a consequence of the time-varying behavior of seismic motion.

The bottom plot in Fig. 8 shows the square root of the cumulative PSD, i.e., the PSD integrated from the highest frequency to DC, where the lowest frequency bin gives the total RMS. The $\mathcal{H}_2$ based controller performs roughly a factor 3 better in terms of RMS with respect to the old controller, resulting from the improved gain in the 0.1 and 0.7 Hz region. In terms of further improvements, the bulk of the contribution to the RMS is above 0.7 Hz, in which it is very difficult to increase the gain due to the restriction of the UGF to at most 2 Hz. Further reduction of the RMS would therefore require increasing the UGF.

6.2. Measured coupling to DARM

The coupling of CARM noise to DARM is also measured and a projection is made of CARM noise to the sensitivity of the detector for both controllers, which is depicted in Fig. 9. The original controller is exactly on the target sensitivity between 10 and 40 Hz, while the new controller spoils the sensitivity below 20 Hz and afterward rolls off significantly.

It is important to note that the coupling is measured before additional measures are taken to reduce the coupling. The reduction of this coupling is done in two steps. First, the mirror actuators are balanced by adjusting their relative gains, after which a subtraction technique is used to subtract CARM noise in DARM [14,24]. With these two additional measures, the coupling is from experience reduced by at least a factor 10 across the 10 to 40 Hz range, since actuator balancing reduces the frequency-independent coupling factor ρ and the noise subtraction is designed to be optimal in this frequency range. This leaves the coupling of both the original controller and the new controller below the target sensitivity by a small factor across the entire frequency range. The choice of 1 percent of coupling between CARM and DARM is thus conservative and the roll-off could be slightly reduced in favor of more robustness margins or a lower RMS if deemed necessary.

It furthermore has to be noted that only the mechanical coupling is assessed in the projection of Fig. 9. The optical coupling due to asymmetries in the optics of the detector is not considered here but is likely the next dominant coupling, particularly above 100 Hz. The shape of K_{RFC} does however not influence this coupling, hence why the optical coupling is not considered in Fig. 9.

7. Conclusion

In this paper, a systematic procedure for the derivation of a noise budget for the laser stabilization loop in AdV+ is presented. The dynamics of the system are modeled using first-principles and a method is given to derive the optical gains of the optical transfer functions experimentally. Combined with the modeled external disturbances, the propagation paths of these disturbances are derived and a noise budget is presented and experimentally verified using data from AdV+. The noise budget allows the identification of the limiting disturbances as well as the effect of the different nested controllers on the propagation of these disturbances to the output of the system. The provided model can furthermore be used to add other disturbances or change current disturbances to determine how these would affect the total noise in the system at each frequency.

Although these noise budgets are indeed used to identify the limiting disturbances as well as how to retune the controller, they are also often under-utilized in this process as the tuning is done by hand based only on insights of the noise budget. This paper therefore also presents a systematic control design procedure that uses $\mathcal{H}_2$ synthesis to derive a $\mathcal{H}_2$ norm optimal controller, in which the noise budget is explicitly used as a weighting function in the optimization. The practical drawbacks of directly using the synthesized controller are solved by using the structure of the $\mathcal{H}_2$ controller and by manually altering the controller until a satisfactory performance is attained. This provides a significantly more structured approach to the control design, which can also be quickly iterated on. Experimental data from the AdV+ detector shows a performance increase of roughly a factor 3 in RMS for the controller derived from the presented method compared to the original manually tuned controller.

The following recommendations are considered relevant for future extensions. The first is to deal more optimally with the lack of stability margins by the controller synthesis. Coping with these still requires design choices that may not necessarily be optimal. Second, implementing hard constraints on for example the controller roll-off could be considered. Presently, the roll-off is manually adjusted using the weighting, but a hard constraint is available once the coupling to the sensitivity is known and a controller could be synthesized to this

constraint. Third, alternative methods of dealing with the time-varying behavior of seismic motion could be considered. Currently, a basic low-order model is used, but more advanced models that are based on e.g., the worst case or mean percentile seismic motion measured on the AdV+ site could be considered.

CRediT authorship contribution statement

Mathyn van Dael: Writing – original draft, Visualization, Methodology, Investigation, Formal analysis. **Julia Casanueva:** Writing – review & editing, Resources, Methodology, Investigation. **Gert Witvoet:** Writing – review & editing, Supervision. **Bas Swinkels:** Writing – review & editing, Supervision. **Diego Bersanetti:** Writing – review & editing, Resources, Investigation. **Manuel Pinto:** Resources, Investigation. **Paolo Ruggi:** Resources, Methodology. **Maddalena Mantovani:** Resources, Investigation. **Camilla de Rossi:** Resources, Investigation. **Piernicola Spinicelli:** Resources, Investigation. **Mattia Boldrini:** Resources, Investigation. **Tom Oomen:** Writing – review & editing, Supervision.

Declaration of competing interest

The authors declare the following financial interests/personal relationships which may be considered as potential competing interests: Mathyn van Dael reports financial support was provided by Netherlands Organisation for Scientific Research (NWO) with grant number 680.92.18.02. If there are other authors, they declare that they have no known competing financial interests or personal relationships that could have appeared to influence the work reported in this paper.

Data availability

The authors do not have permission to share data.

Acknowledgments

The authors gratefully acknowledge the Italian Istituto Nazionale di Fisica Nucleare (INFN), the French Centre National de la Recherche Scientifique (CNRS) and the Netherlands Organization for Scientific Research, for the construction and operation of the Virgo detector and the creation and support of the EGO consortium. The authors also gratefully acknowledge research support from these agencies as well as by the Spanish Agencia Estatal de Investigación, the Consellera d'Innovació, Universitats, Ciència i Societat Digital de la Generalitat Valenciana and the CERCA Programme Generalitat de Catalunya, Spain, the National Science Centre of Poland and the Foundation for Polish Science (FNP), the European Commission, the Hungarian Scientific Research Fund (OTKA), the French Lyon Institute of Origins (LIO), the Belgian Fonds de la Recherche Scientifique (FRS-FNRS), Actions de Recherche Concertées (ARC) and Fonds Wetenschappelijk Onderzoek – Vlaanderen (FWO), Belgium. This work is also part of the research program VIDI with project number 15698, which is (partly) financed by the Netherlands Organisation for Scientific Research (NWO).

References

[1] F. Acernese, et al., Advanced Virgo Plus: Future perspectives, J. Phys. Conf. Ser 2429 (2023) 012040.
[2] D. Bersanetti, B. Patricelli, O.J. Piccinni, F. Piergiovanni, F. Salemi, V. Sequino, Advanced Virgo: Status of the detector, latest results and future prospects, Universe 7 (2021).
[3] A. Buikema, et al., Sensitivity and performance of the Advanced LIGO detectors in the third observing run, Phys. Rev. D 102 (2020) 062003.
[4] F. Acernese, et al., Laser with an in-loop relative frequency stability of 1.0×10^{-21} on a 100-ms time scale for gravitational-wave detection, Phys. Rev. A 79 (2009) 053824.
[5] E. Capocasa, Optical and Noise Studies for Advanced Virgo and Filter Cavities for Quantum Noise Reduction in Gravitational-Wave Interferometric Detectors Ph.D. thesis, Universite Paris Diderot, 2017.
[6] J. Casanueva Diaz, Control of the Gravitational Wave Interferometric Detector Advanced Virgo Ph.D. thesis, Université Paris-Saclay, 2017.
[7] D. Thomas, V. Mohit, C. Christophe, Complementary filters shaping using $\mathcal{H}_2$ synthesis, in: 2019 7th International Conference on Control, Mechatronics and Automation, ICCMA, 2019, pp. 459–464.
[8] D. Schütte, Modern Control Approaches for Next-Generation Interferometric Gravitational Wave Detectors Ph.D. thesis, Gottfried Wilhelm Leibniz Universität Hannover, 2016.
[9] L. Trozzo, Low Frequency Optimization and Performance of Advanced Virgo Seismic Isolation System Ph.D. thesis, Università degli Studi di Siena, 2018.
[10] M.G. Beker, A. Bertolini, J.F.J. van den Brand, H.J. Bulten, E. Hennes, D.S. Rabeling, State observers and Kalman filtering for high performance vibration isolation systems, Rev. Sci. Instrum. 85 (2014) 034501.
[11] K.S. Karvinen, D. Schütte, B. Schulte, M. Heurs, Optimal Control of a Triple Pendulum Mirror Suspension for a Gravitational Wave Detector: New Insights for Reducing Mirror Displacement Noise, Technical Report, Max Planck Institut für Gravitationsphysik (Albert Einstein Institut, Hannover, Germany, 2016.
[12] M. van Dael, G. Witvoet, B. Swinkels, M. Pinto, J. Casanueva, D. Bersanetti, M. Mantovani, M. Vardaro, T. Oomen, Design for interaction: Factorized Nyquist based control design applied to a gravitational wave detector, in: Proceedings of the 2022 Modelling, Estimation and Control Conference, 2022.
[13] E.D. Black, An introduction to Pound–Drever–Hall laser frequency stabilization, Am. J. Phys. 69 (2001) 79–87.
[14] T. Accadia, et al., Performance of the Virgo interferometer longitudinal control system during the second science run, Astropart. Phys. 34 (2011) 521–527.
[15] E. Calloni, G. Vajente, Conceptual Design of the Second Stage of Frequency Stabilization for Advanced Virgo, Technical Report VIR-0013C-12, EGO, 2012.
[16] C. Cahillane, G. Mansell, Review of the Advanced LIGO gravitational wave observatories leading to observing run four, Galaxies 10 (2022).
[17] K. Numata, A. Kemery, J. Camp, Thermal-noise limit in the frequency stabilization of lasers with rigid cavities, Phys. Rev. Lett. 93 (2004) 250602.
[18] S. Braccini, et al., Measurement of the seismic attenuation performance of the VIRGO superattenuator, Astropart. Phys. 23 (2005) 557–565.
[19] I. Fiori, Reference Seismic Data for Virgo, Technical Report VIR-0390A-15, The Virgo Collaboration, 2015, https://tds.virgo-gw.eu/ql/?c=11118.
[20] F. Ardhuin, L. Gualtieri, How ocean waves rock the earth: Two mechanisms explain microseisms with periods 3 to 300 s, Geophys. Res. Lett. 42 (2002) 765–772.
[21] J.C. Doyle, Guaranteed margins for LQG regulators, IEEE Trans. Autom. Control 23 (1978) 756–757.
[22] S. Skogestad, I. Postlethwaite, Multivariable Feedback Control: Analysis and Design, John Wiley & Sons, West Sussex, United Kingdom, 2005.
[23] J. Doyle, K. Glover, P. Khargonekar, B. Francis, State space solution to standard H2 and H∞ control problem, IEEE Trans. Autom. Control 34 (1989) 831–847.
[24] G. Vajente, Analysis of Sensitivity and Noise Sources for the Virgo Gravitational Wave Interferometer Ph.D. thesis, Scuola Normale Superiore di Pisa, 2008.